Reliability Investigation of Silicide-Based Thermoelectric Modules

Mahdi Mejri, Krunoslav Romanjek, Hilaire Ihou Mouko, Yohann Thimont, Mostafa Oulfarsi, Nicolas David, Benoît Malard, Claude Estournès, Anne Dauscher

Reliability investigation of silicide-based thermoelectric modules

Journal:	*ACS Applied Materials & Interfaces*
Manuscript ID	am-2023-15429t.R2
Manuscript Type:	Article
Date Submitted by the Author:	15-Jan-2024
Complete List of Authors:	MEJRI, Mahdi; CIRIMAT, ROMANJEK, Krunoslav; CEA LITEN IHOU-MOUKO, Hilaire; HotBlock OnBoard Thimont, Yohann; CIRIMAT Oulfarsi, Mostafa; IJL DAVID, Nicolas; Université de Lorraine, Institut Jean Lamour Malard, Benoit ; CIRIMAT Estournes, Claude; CIRIMAT Dauscher, Anne; Institut Jean Lamour, UMR 7198 CNRS-Université de Lorraine

Graphical abstract

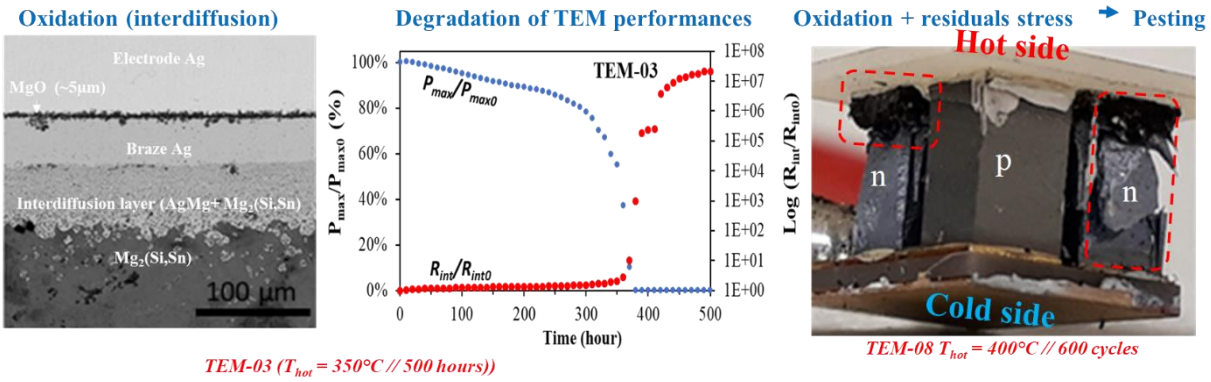

Reliability investigation of silicide-based thermoelectric modules

Mahdi Mejri[a], Krunoslav Romanjek[b], Hilaire Ihou Mouko[c], Yohann Thimont[a], Mostafa Oulfarsi[d], Nicolas David[d], Benoît Malard[e], Claude Estournès[a], Anne Dauscher[d]*

[a]*CIRIMAT, Université de Toulouse, CNRS, Université Toulouse 3 - Paul Sabatier, 118 Route de Narbonne, 31062 Toulouse cedex 9 – France*

[b]*Université Grenoble Alpes, CEA-LITEN, 17 rue des Martyrs, Grenoble Cedex 30054, France*

[c]*HotBlock OnBoard (HBOB), 43 Chemin du Vieux Chêne, 38240 Meylan, France*

[d]*Université de Lorraine, CNRS, Institut Jean Lamour, F-54000 Nancy, France*

[e]*CIRIMAT, Université de Toulouse, CNRS, INP- ENSIACET - 4 allée Emile Monso BP44362, 31030 Toulouse cedex 4 – France*

**Corresponding authors: mahdi.mejri@toulouse-inp.fr (Mahdi MEJRI)*

Abstract

The reliability and failure mechanisms of silicide based thermoelectric modules (*n*-type $Mg_2(Si,Sn)$ / *p*-type HMS) were investigated thanks to two types of thermal tests with either a fixed or a cycling thermal gradient, under different atmospheres. The hot interfaces of the thermoelectric modules were analyzed by scanning electron microscopy and X-ray diffraction, after the reliability tests. The current thermoelectric modules do not exhibit any failure mechanism under ambient air for a hot side temperature of 250°C for tests conducted either during 500 hours at a fixed temperature gradient or after 1000 thermal cycles. However, when the temperature was increased to 350°C, pesting phenomena were detected at the hot side of the *n*-type $Mg_2(Si,Sn)$ legs caused by the decomposition/oxidation of the material. These phenomena are strongly slowed down for thermoelectric modules tested under primary vacuum, highlighting the predominant role of oxygen in the degradation mechanism. Interdiffusion phenomena are the most pronounced at the interface of the hot side of the *n*-type thermoelectric materials. The formation of a MgO layer, which is an electrical and thermal insulator, has decreased the thermoelectric modules performances. For thermal cycling tests, cracks are observed on the hot side of the n-type legs. The presence of these cracks drastically increases the thermal and electrical resistances, leading to an overheating of the system, limiting its efficiency and failure by breaking electrical continuity. The interfaces at the hot side temperature of the *p*-type HMS legs remained intact whatever the test conditions were, indicating a high chemical stability and a good mechanical strength.

Keywords:
Thermoelectric Module Reliability, Pesting, Oxidation, Higher Manganese Silicide, Magnesium Silicide

1. Introduction

The global development of the human activity involves an increase in greenhouse gas emissions leading to a rise in temperature and to climate change. Reaching the ambitious project of achieving the carbon neutrality by the middle of the 21th century needs to replace the fossil energies by any other source of energy issued from nuclear energy or renewable energies, mainly solar, wind, or hydraulic. The use of thermoelectricity may be also a clean alternative solution because of its numerous advantages. While it allows exploiting the large amounts of waste heat in our atmosphere by transforming them directly into useful electricity, no use of toxic elements is needed [1]. Compared to conventional technologies, such as heat engines, the conversion of energy via thermoelectric generators (TEGs) is direct, without mobile parts and autonomous. TEGs can be used for both micro-power generation (e.g. mobile applications) and kilowatt production (e.g. industrial applications) [2,3]. The thermoelectric technology has been used for years for powering space missions far from the sun because of their high reliability without any maintenance and their long lifetime. However, the conversion efficiencies remain relatively low and depend on the performance of the used thermoelectric (TE) materials [4].

Over the last five decades, *n*-type higher manganese silicides (HMS) and *p*-type magnesium silicides, such as $MnSi_{\gamma}$ ($1{,}71 \leq \gamma \leq 1{,}78$) [5–10] and $Mg_2(Si,Sn)$ [11–15], respectively, have been found to be very promising TE materials for medium temperature applications (230-530 °C). They are eco-friendly and are composed of abundant and cheap materials, while exhibiting a high TE performance. Many studies have been focused on the manufacturing and development of silicium-based TEGs [14–20]. Stability problems caused by oxidation may however hinder the use of the $Mg_2(Si,Sn)$ solid solutions in long-term applications at high temperature [21–28]. On the other hand, HMS exhibit good chemical, thermal and mechanical stability [29–34]. In a previous work [14], we have shown that silicide-based thermoelectric modules (TEM), composed of *n*-type ($Mg_2Si_{0.6}Sn_{0.4}$) and *p*-type ($MnSi_{1.77}$) legs and manufactured on the base of 'half skeleton', exhibit no deterioration during the performance test carried out up to 450 °C. An average maximum power output of 0.37 W, corresponding to a power density of 0.95 W/cm^2, has been achieved for a temperature difference of 400 °C (hot side temperature of 450 °C). Long term reliability tests are however essential to validate our design, as under usual conditions of service, the TEM are exposed to high thermal amplitude, high thermal gradients (e.g. hundreds of °C/cm) and a long period of cycling depending on the seeked application (e.g. automotive, aeronautics, etc.) [35–37]. Such conditions lead to a high thermal stress in TEM which can lead to their failure, particularly at their hot side where diffusion, interdiffusion and thermo-migration phenomena are more frequent. This degradation is even more accelerated when the materials

layers (braze, metallization, ...) used at the hot interface are thin with regard to thicker layers, as the heat transfer and thus interdiffusion phenomena are more important.

Moreover, during thermal application, TEM are subjected to thermomechanical stresses at all interfaces (i.e. on both hot and cold sides of the TEM), due to the thermal expansion coefficients mismatch of the materials used in the manufacturing of the system (i.e.: Ag, AlN, Cu and TE materials) that may lead to cracks [38,39]. The presence of these cracks drastically increases the thermal and electrical resistances, leading to an overheating of the system, limiting its efficiency and failure by breaking electrical continuity.

Thermal management is crucial for ensuring optimal performance and reliability of power modules. Fixed temperature and cycling thermal tests are two common methods used to evaluate the thermal behavior of TEM. Fixed temperature tests provide a simple and quick evaluation of a power module's thermal performance under steady-state conditions, whereas cycling thermal tests can provide a more realistic assessment of the module's performance under dynamic thermal conditions. In this paper, we present the reliability investigation of our silicide-based TEM. Reliability tests were performed under different atmospheres and thermal gradients in order to evaluate the temperature domain in which our TEM are able to operate without failure and also to characterize the failure mechanisms.

2. Materials and methods

2.1. Module design and manufacturing

The TEM used in this work were manufactured by the HotBlock OnBoard (HBOB) company (Meylan, France,). Their architecture, already described in reference [15], is recalled in Figure 1.a. A TEM consists of two *n*-type ($Mg_2Si_{0.6}Sn_{0.4}$) and *p*-type ($MnSi_{1.77}$) couples sandwiched between a DBC (direct bonding copper) ceramic substrate (AlN) and a silver (Ag) electrode. The metallization layers of the hot and cold sides are constituted of Ti (30 nm)/Au (335 nm). The TEM is assembled by brazing with Ag. A complete description of their design, assembly, and TE performances has been reported in [15]. Detailed studies of the *n*-type et *p*-type raw materials and legs properties, such as for instance microstructure, chemical composition, mechanical properties and stability under air, were already reported in our last papers [15,27,28,40,41]. In the rest of this paper, we will refer to $MnSi_{1.77}$ as HMS and $Mg_2Si_{0.6}Sn_{0.4}$ as $Mg_2(Si,Sn)$.

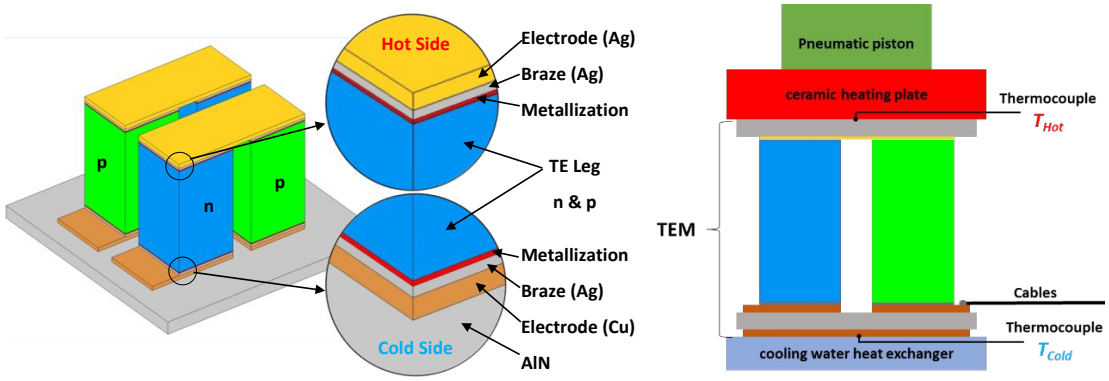

Figure 1. (a) TEM 3D architecture. TE legs dimensions are 3 × 3 × 4.6 mm³. Spacing between TE legs is 1 mm. The thicknesses of the electrode and the braze are 125 µm and about 30 µm respectively. (b) Schematic bench test.

2.2. Performance testing

As the different fabricated TEM showed a very good performances reproducibility [15], some of them were chosen randomly to test their ability to resist mechanically and chemically under thermal stress, under temperature and atmospheric conditions most representative of real conditions of work. All reliability tests were carried out on the test bench used for measuring the electrical performances of the TEM in [15], developed in [42]. It is schematized on Figure 1.b. The TEM is placed between a cooled water heater exchanger (cold side (AlN)), and a ceramic heater plate (hot side, Ag electrode). To improve the thermal contact, a controlled pressure of 10 bars is applied to the TEM via a pneumatic piston located above the ceramic heating plate. For the temperature measurements, thermocouples were placed on the contact surface between the hot/cold side of the TEM and the two plates of the bench test. Two types of thermal tests, with fixed or cycling thermal gradient, were conducted under different atmospheres.

For fixed thermal gradient tests, the internal resistance (R_{int}) and the maximum power (P_{max}) were measured every 10 hours. P_{max} was calculated from R_{int}, the open circuit voltage (V_{OC}) and the current (I). $R_{int,0}$ and $P_{max,0}$ are the initial values of the internal resistance and the maximum power before the reliability test, respectively. The cold side of the TE is kept at 50°C during all tests while the hot side is kept at a constant temperature of either 250 or 350°C during a given duration.

For cycling thermal gradient tests, a 3 minutes delay is applied to stabilize the thermal gradient before the measurement of the current-voltage performance. It allows to follow the evolution of the performance cycle by cycle under the same conditions, at stable temperature values. The internal resistance (R_{int}) and the maximum power (P_{max}) were measured every 15 minutes. The cold side of the TEM is maintained at 50°C in all tests. The temperature of the hot side varies between 150°C and the maximum applied value, i.e. 250, 350 or 400°C.

The test bench is equipped with a sealed chamber connected to a pump allowing to reach a primary vacuum. For primary vacuum, a pumping was performed until reaching the minimum pressure (1 mbar) followed by a refilling with N_2 (5.0) until reaching 20 mbar. This step (pumping + refilling) was performed only once for TEM-03, TEM-9, TEM-07, TEM-08 and 4 times for TEM-04*. In Table 1 are summarized the thermal and atmosphere conditions for reliability tests performed on 8 selected TEMs from [15].

Table 1. Summary of the TEM reliability test conditions.

Thermal gradient	TEM number	T_{cold} (°C)	T_{hot} (°C)	$R_{int.0}$ (Ω) [15]	$P_{max.0}$ (W) [15]	Atmosphere
Fixed	01	50	250	0.056	0.064	ambient
	02	50	350	0.061	0,183	ambient
	03	50		0.062	0.178	Primary vacuum
	04	50		0.059	0.173	Primary vacuum*
Cycling	05	50	150 ↔ 250	0.510	0.074	ambient
	06 & 07	50	150 ↔ 350	0.056	0.167	Primary vacuum
	08	50	150 ↔ 400	0.059	0.255	Primary vacuum

2.3. Contact resistance measurement

Contact resistance (Rc) measurements were performed by the 3-points transmission line method (TLM) using a bench test developed at the CIRIMAT lab. The aim was to determine the evolution of the contact resistance between the metallized legs and the brazed metallic tracks. The bench test is constituted of a micro-positioner (sensitivity of 1 µm) to move a probe (for the voltage measurement) and of a microscope to visualize the location of the probe in contact with the sample surface. The sample is placed in a clamp with two electrodes applying a current of 100 mA across the legs. The contact pressure of the clamp is controlled by a spring/screw

system. The voltage measurements were performed on parallelepiped samples of 6 x 6.5 mm^2 in section. This is a series assembly connected of two metallized TE legs (5 mm in thickness), placed between copper electrodes (0.8 mm in thickness). The sample is described in the Figure 2.c. The assembly was carried out with Ag braze (about 50 µm) under the same assembly conditions as those used to manufacture the TEM [15]. The contact resistance values were calculated according to the equations described in paper [43].

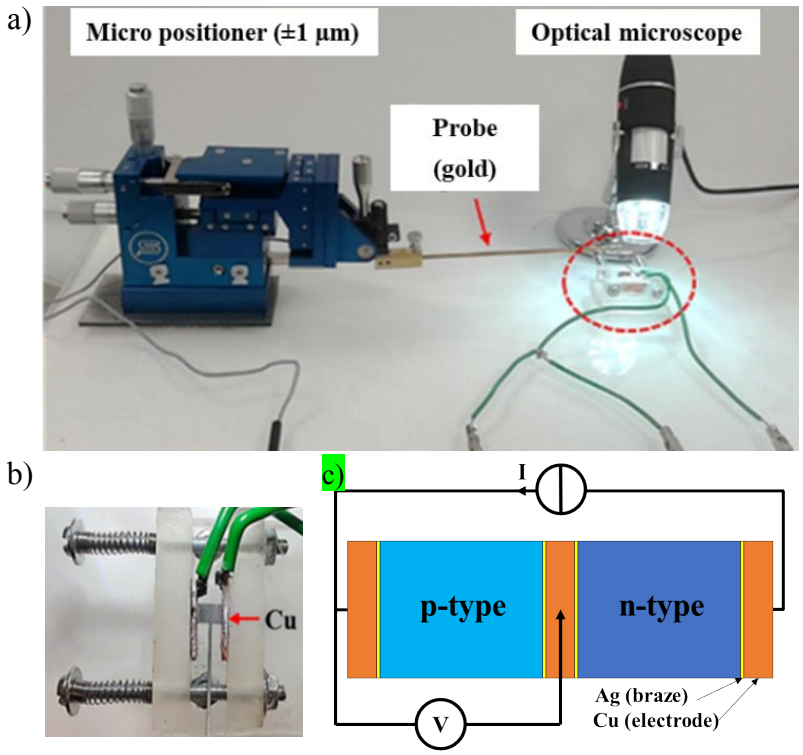

Figure 2. (a) Bench test of contact resistance measurement for a brazed assembly. (b) Sample fixation clamp with a simple leg. (c) Scheme of contact resistance measurements of Cu/p-type-leg/Cu/n type-leg/Cu brazed sample via TLM.

2.4. High-energy X-ray diffraction

High-energy X-ray diffraction (HEXRD) experiments were performed at PETRA III-DESY-Hamburg on the P07-B beamline. The measurements were performed with a 103.4 keV (λ = 0.119987 Å) monochromatic beam with size of 2 x 300 μm^2. The high energy beam allowed us to analyze a large volume of the sample (i.e., 2 x 300 x 3000 μm^3 per acquisition point). The emitted signal was collected by a large area (41 x 41cm^2) Perkin Elmer 2D detector that recorded the entire Debye-Scherrer rings with a maximum angle of 2θ = 12° (Figure 3.a).

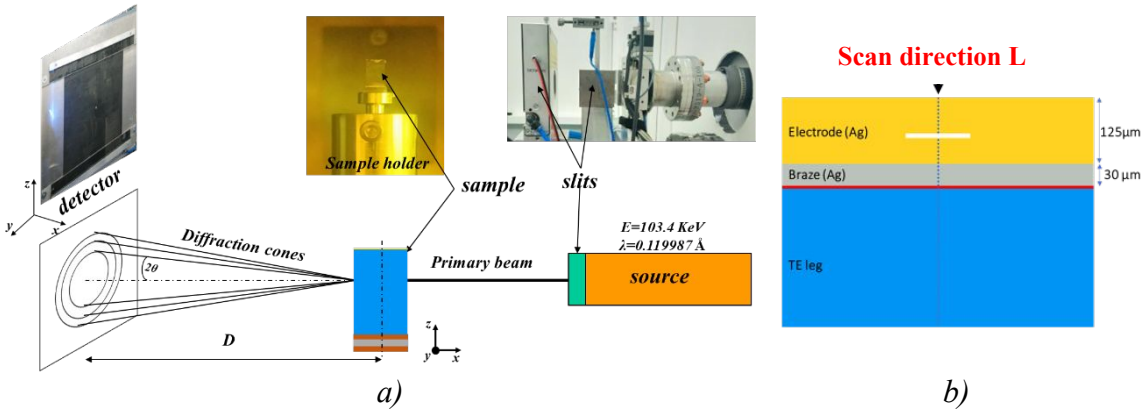

Figure 3. (a) Schematic of the synchrotron high-energy X-ray diffraction experimental setup. (b) Scan direction of the synchrotron beam (in white, the spot is 2 x 300 µm² in section) along the TEM.

The acquisition scans were performed along line L in z-direction (Figure 3.b) with an acquisition speed of 1 µm/s. In order to center the specimen and align the beam with the top surface of the sample, a series of absorption and reflective scans were made by using the direct beam and a photodiode positioned behind the sample. The 2D detector to sample distance (D = 1.5 m) and the detector tilts were calibrated using a cerium dioxide powder diffraction standard from NIST (CeO_2 – SRM 674b) and pyFAI software suite [44]. A similar setup has been used in references [45,46].

3. Results and discussion

3.1. Thermoelectric modules performances

3.1.1. Fixed thermal gradient

3.1.1.1. Fixed gradient test with T_{hot}=250°C

The hot side of TEM-01 was maintained at 250°C for 500 hours under ambient air. The evolution with time of R_{int} and P_{max} is shown in Figure 4.a. The maximum power P_{max} is stable (variation < 1%) during all the time. On the other hand, a slight increase of the internal resistance R_{int} (+ 10.6%) is detected. This increase can be explained by the stabilization of the TE properties of the materials with time (simultaneous increase of the electrical resistivity and of the Seebeck coefficient) as well as by the stabilization of the contact surfaces during the test. It is caused by reinserting the TEM after initial diffusion bonding (braze-on bonding) of the hot side. Similar results were reported by Skomedal et al. [14]. After the test, TEM-01 appears visually intact with no signs of macroscopic degradation (Figure 4.b). This reliability test shows that our silicide based TEM resist under air at 250°C and indicates that, with a Maximum Power Point Tracking system (MPPT), the TEM will remain efficient in a TEG.

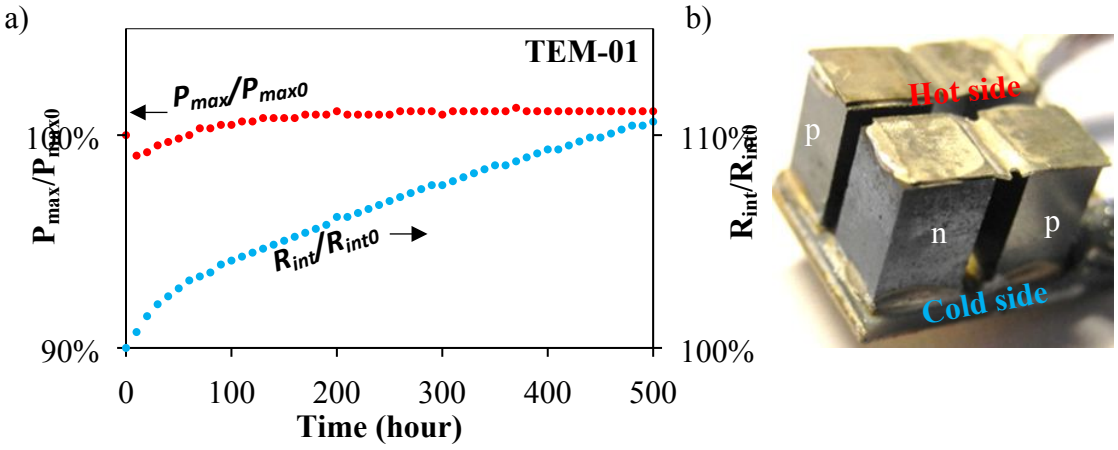

Figure 4. (a) Relative variation of R_{int} (blue) and P_{max} (red) during the fixed thermal gradient test of the TEM-01 (T_{hot}= 250°C & T_{cold} = 50°C). (b) Photography of TEM-01 after the reliability test.

3.1.1.1. Fixed gradient test with T_{hot}=350°C

To take advantage of the TE power increase with temperature of the *n*- and *p*-type materials [15], and thus to increase the power delivered by the TEM, similar tests were carried out with the hot side maintained at 350°C. TEM-02 and TEM-03 were tested for 500 hours under ambient air (P_{total} = 0.9 bar) and under primary vacuum, respectively. During the first 300 hours of testing, R_{int} gradually increases with a slight decrease in the maximum power P_{max} (Figure 5). After 300 hours, a drastic increase of R_{int} is measured until the complete loss of the electrical contact in a few tens of hours. At the same time, P_{max} began to decrease more promptly until an important decline during the last ten hours of the test.

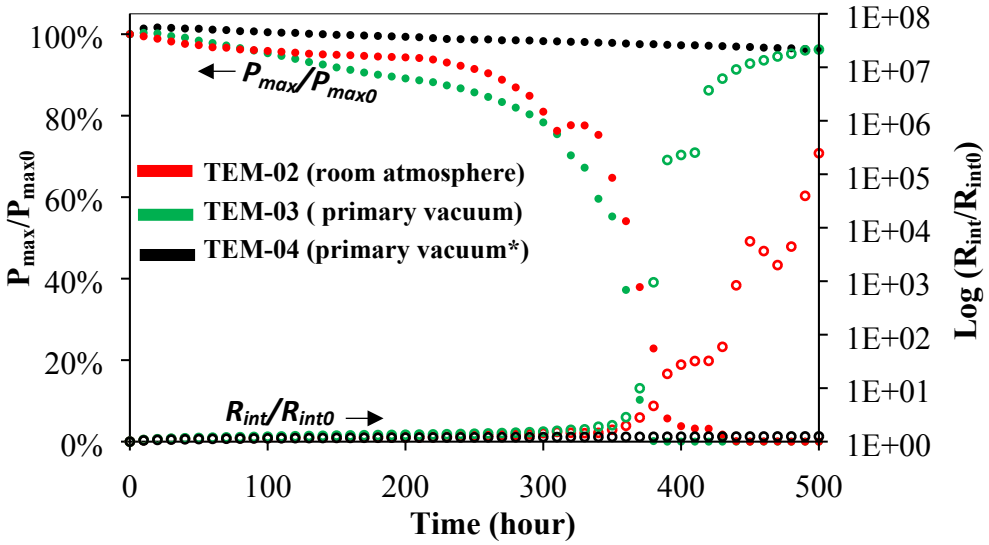

Figure 5. Variation of R_{int} (open circle) and P_{max} (close circle) during thermal test of TEM-02 (red), TEM-03 (black) and TEM-04 (green) (T_{hot}= 350°C & T_{cold} = 50°C).

As shown in the Figure 6.a, only the *n*-type legs are deteriorated at the hot side of TEM-02 (ambient air test), presenting a black porous delaminated layer and cracks. This black porous

layer is mainly constituted of magnesium oxide (MgO), as shown on the X-ray diffraction (XRD) pattern from this powder (Figure 6.d). It results from the oxidation of Mg, leading to the decomposition of the *n*-type $Mg_2(Si,Sn)$ material. The degradation of the TEM performances during the thermal test is related to the gradual slow degradation of the hot interfaces of the *n*-type material. The MgO layer, which is an electrical insulator, is progressively forming during the first 300 h in service, explaining the slow increase of the $R_{int.}$ The presence of this layer, also thermal insulator, explains the decrease of P_{max} by decreasing the thermal gradient on both sides of the *n*-type TE legs. After 300 h, due to strong material degradation, the electrical properties could not be measured anymore. The hot interfaces of the *p*-type legs remain intact, indicating a higher chemical stability and a better mechanical strength of these legs under these test conditions.

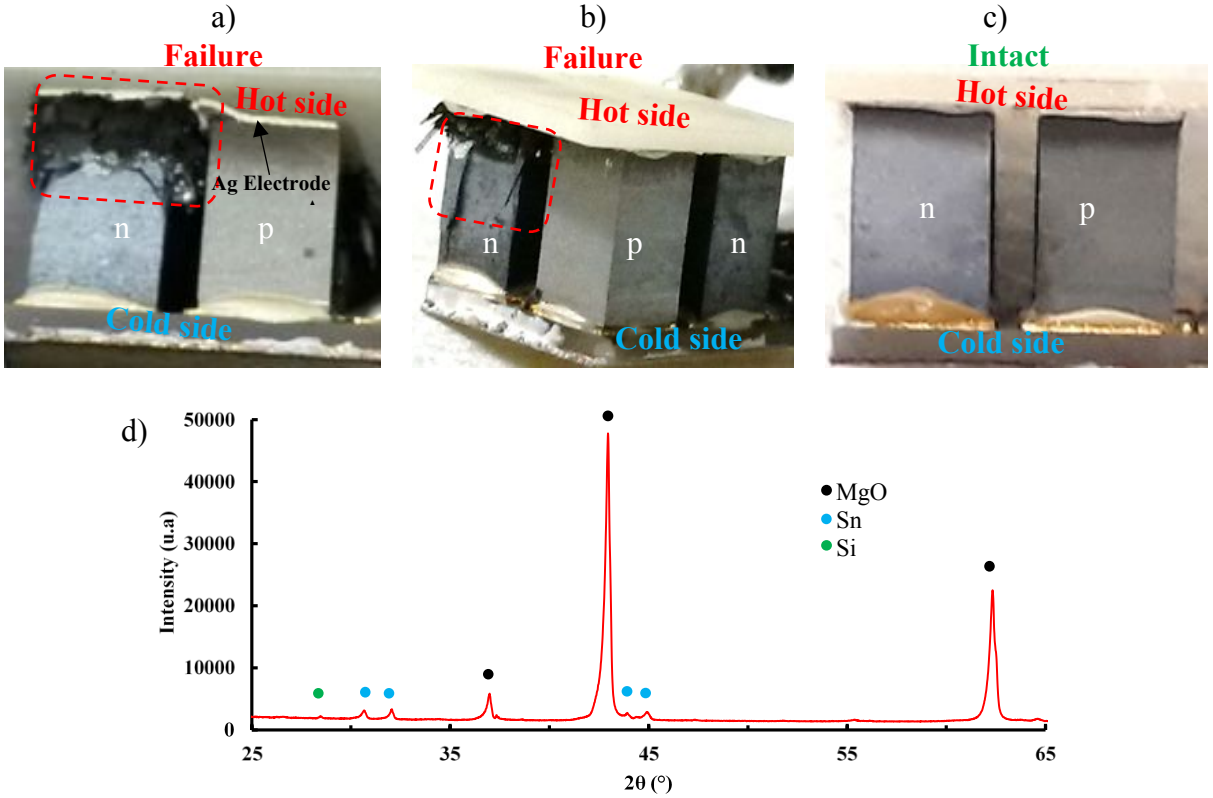

Figure 6. (a) TEM-02, (b) TEM-03 and (c)TEM-04 after reliability tests. (d) XRD pattern of the black porous layer issued from the n-type leg decomposition of TEM-02 (λ_{Cu} = 1.541 Å).

In contrast to TEM-02, only one of the two *n*-type legs appears to be damaged for the TEM-03 (Figure 6.b), while the second one appears intact with no apparent sign of macroscopic damage. However, cross sectional analysis (Figure 7.a) revealed a thin layer of 5 µm of MgO between the electrode (Ag) and the braze (Ag) at the hot interface of the intact n-type leg. This layer is detected all along the braze/electrode interface. The migration of Mg, driven by a high thermal gradient, has favored the formation of MgO between the electrode (Ag) and the braze where an

important porosity remains. The presence of MgO at the interface impacts significantly the R_{int} and P_{max} in an unfavorable way since the latter is a good electrical and thermal insulator. On the other hand, as shown in the Figure 7.a, a thick diffusion layer (~ 80 µm) was formed between the TE legs and the braze due to the silver (braze Ag) and magnesium (Mg) interdiffusion. In this layer, the MgAg and MgO phases were detected by XRD analyses (Figure 7.b). The solid solution MgAg was also detected by Pham et al. using Ag as an electrode [47].

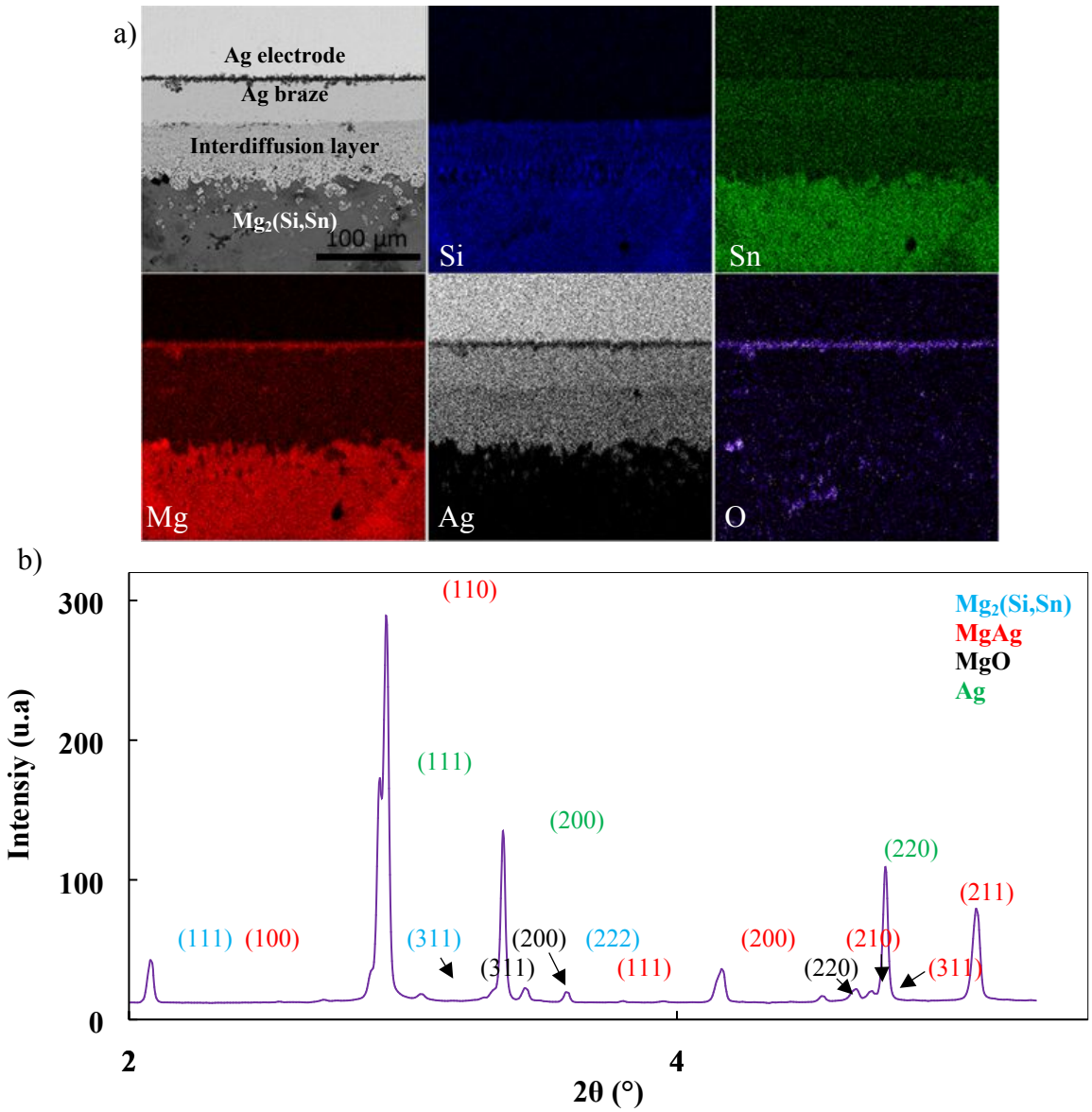

Figure 7.(a)SEM/EDS mapping of cross section of n-type hot side of TEM-03. The analysis was performed at the center of the overlap line of the brazed joint. (b) HEXRD pattern of n-type hot side of TEM-3 in the interdiffusion layer mentioned in Figure 7.a (Analysis volume was 2 x 300 x 3000 µm³).

Tests performed under these operating conditions induce a significant failure of the $Mg_2(Si,Sn)$ leg of our TEM. The temperature is a catalyst for diffusion phenomena on the hot side of the TEM. Two papers have experienced the same degradation phenomena on silicide-based TEM

[27,36]. The decomposition of the $Mg_2(Si,Sn)$ solid solution is known in the literature as "pesting" [48,49]. The accommodation of residual stress coupled with oxidation lead to brittle fracture and a total degradation of TEM performances [27].

As shown in the Figure 5, the maximum power P_{max} of TEM-04 is unchanged (< 3%) and a only a slight increase of the internal resistance R_{int} (+ 15%) is detected. These results are very close to those of TEM-01. TEM-04 displays a good chemical and mechanical stability during the test and no apparent signs of damage is observed (Figure 6.c).

For TEM-04, diffusion and oxidation phenomena have been significantly reduced in a proper chamber in which the oxygen saturation is low. This reliability test showed that our TEM could resist at 350°C under use of primary vacuum and indicates that with a MPPT system, the TEM would remain efficient in a TEG. As demonstrated in our previous paper [15], the TEM-04 delivers 0.51 W/cm² (per module area) with T_{hot} = 350°C. This power is 2.5 higher than the power reached in TEM-01 (for which T_{hot} was only 250°C). This result is in agreement with the fact that the optimal of figure of merit (ZT) of these silicide materials are in intermediate temperature range (400°C).

3.1.2. Thermal cycling

3.1.2.1. Cycling test with T_{hot}=250°C

For TEM-05, a thousand of thermal cycles of 15 min dwell time was applied under ambient air, the temperature of the hot side of the TEM being varied between 150°C and 250°C, the temperature at the cold side being maintained at 50°C. P_{max} as well as R_{int} increase slightly with increasing the number of cycles (+3.4% and +4.8%, respectively, Figure 8.a). These behaviors are similar to those observed with TEM-01 and can be explained by the same effects (stabilization of the TE properties of the materials, stabilization of the contact surfaces.

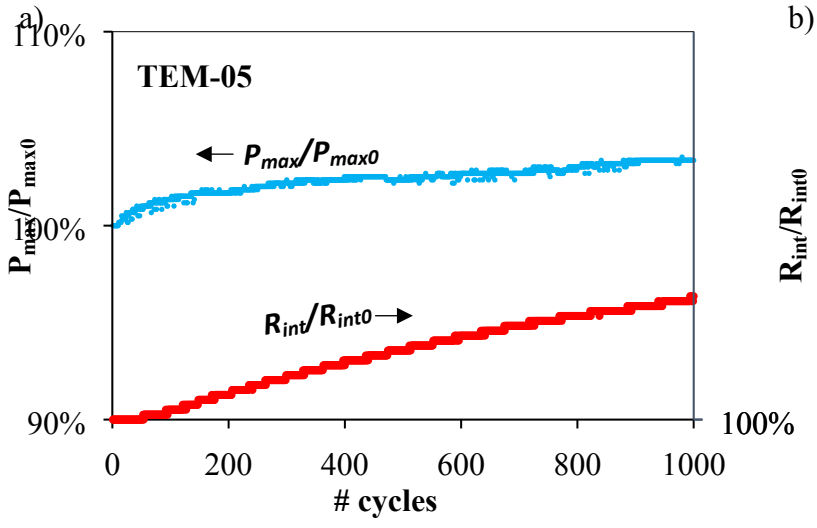

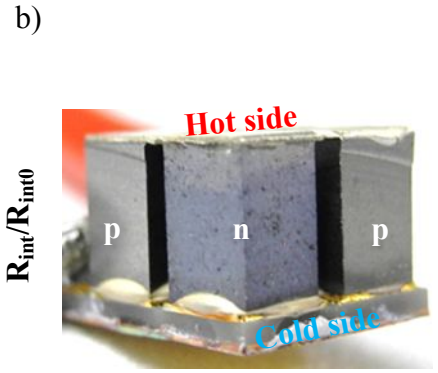

c)

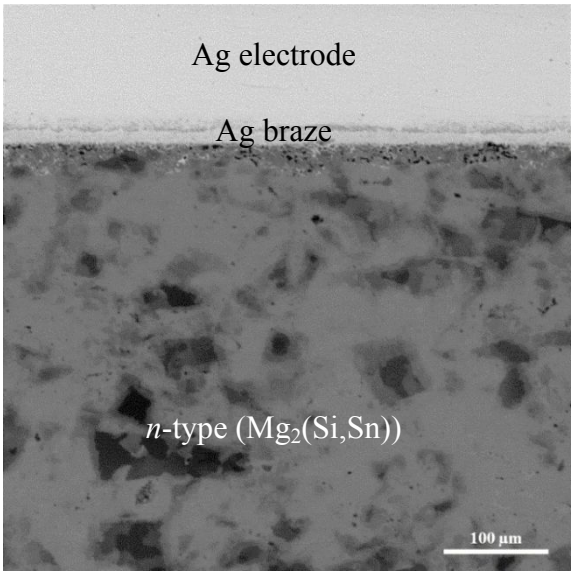

Figure 8. (a) Variation of R_{int} (red) and P_{max} (blue) during 1000 thermal cycling tests of TEM-05 (T_{hot}= 150°C-250°C & T_{cold} = 50°C). (b)Photography of TEM-05 after the reliability test. (c) SEM of the cross section of the n-type material at the hot side of TEM-05. The analysis was performed at the center of the overlap line (Figure 3) of the brazed joint after reliability test .

TEM-05 seems to appear intact after 1000 cycles (Figure 8.b). None macroscopic sign of degradation can be observed. The hot interface of the *n*-type TE leg of the TEM-05 has been checked by SEM after the test (Figure 8.c). The interface (electrode/braze/TE legs) exhibits no degradation and displays a good homogeneity and integrity. Our TEM resist under the conditions tested and indicates that with a MPPT system, the TEM will remain efficient. Nevertheless, this temperature remains too low to take full advantage of the TE properties of the silicide materials used. The maximum power delivered by the TEM is around 0.21 W/cm^2 (per module area).

3.1.2.2. Cycling test with T_{hot}=350°C

Thermal cycling tests (1000 cycles) were carried out on TEM-06 and TEM-07, the temperature on the hot side of the TEM being varied between 150°C and 350°C. The tests were performed under primary vacuum (pumping until reaching the minimum pressure (1 mbar) followed by a nitrogen filling until reaching 20 mbar) to slow down the oxidation phenomena observed for TEM-02 and TEM-03. The variations of R_{int} and P_{max} as a function of number of cycles of TEM-06 and TEM-07 are reported on Figure 9.a. A slight and monotonous decrease of P_{max} is noticed. After the thermal cycling test, the two TEM appear intact and show no signs of macroscopic degradation (Figure 9.b).

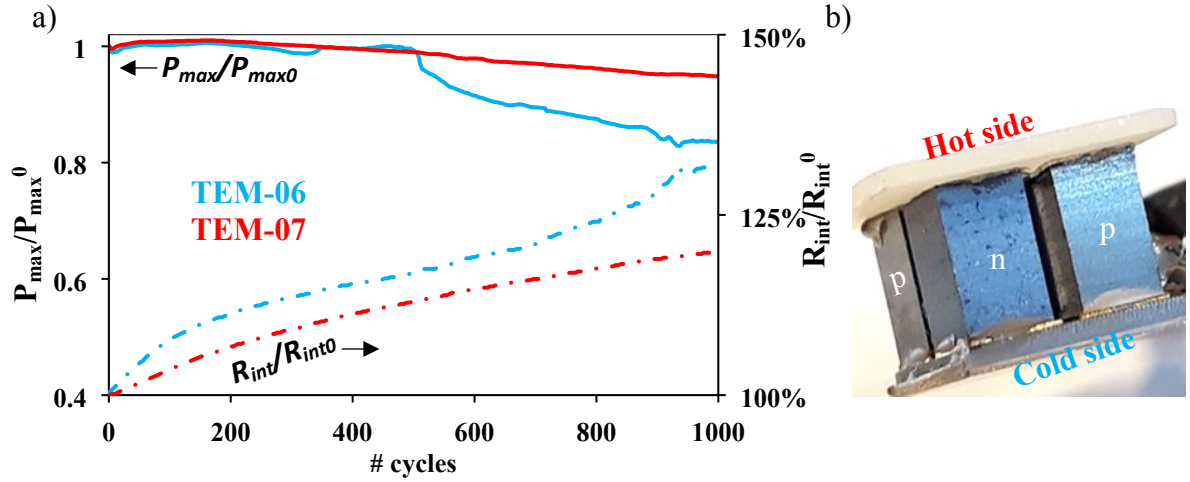

Figure 9.(a) Variations of R_{int} (doted line) and P_{max} (continuous line) during thermal cycling tests of TEM-06 and TEM-07 (T_{hot}= 150°C-350°C & T_{cold} = 50°C) (b) TEM-06 after the reliability test.

SEM pictures of the hot interface of the *n*-type TE of TEM-06 and TEM-07 are presented in Figures 10 and 11, respectively. For TEM-06, a layer of about 7 µm of MgO is observed between the electrode (Ag) and n-type TE material. This layer is detected all along the braze/electrode interface, similarly to what was observed with the temperature test at constant temperature. On the other hand, a thick diffusion layer (~ 20 µm) was formed between the TE leg and the solder. In this layer, as previously observed in TEM-03, an MgAg phase is formed between the braze and the n-type TE material caused by the mutual interdiffusion of Ag and Mg. The two diffusion layers are highlighted by XRD (Figure 10.c).

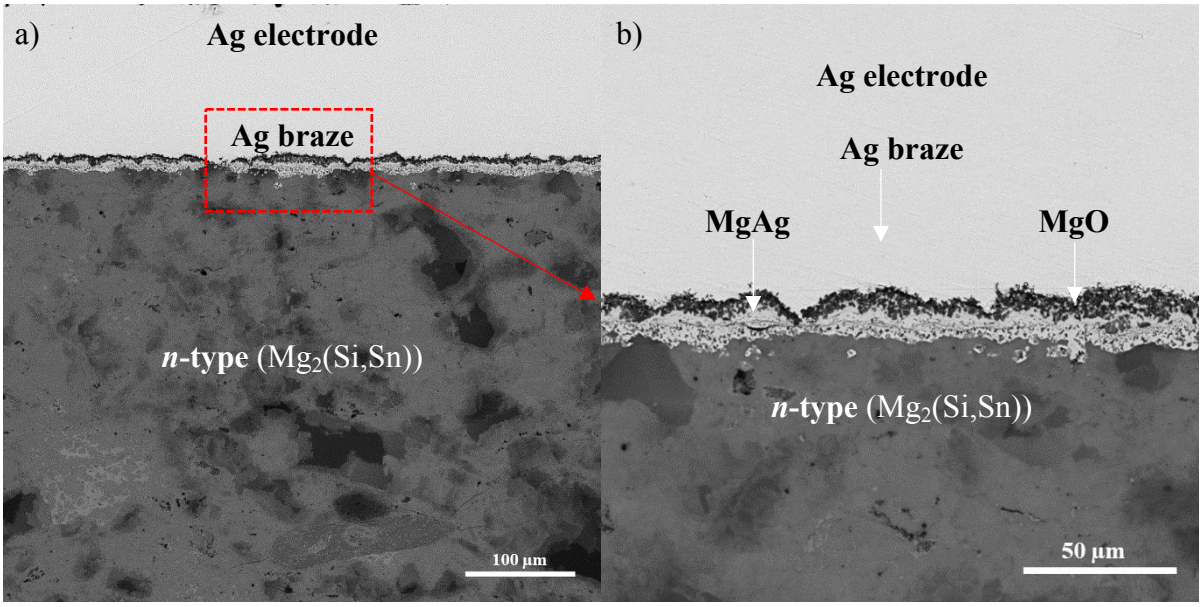

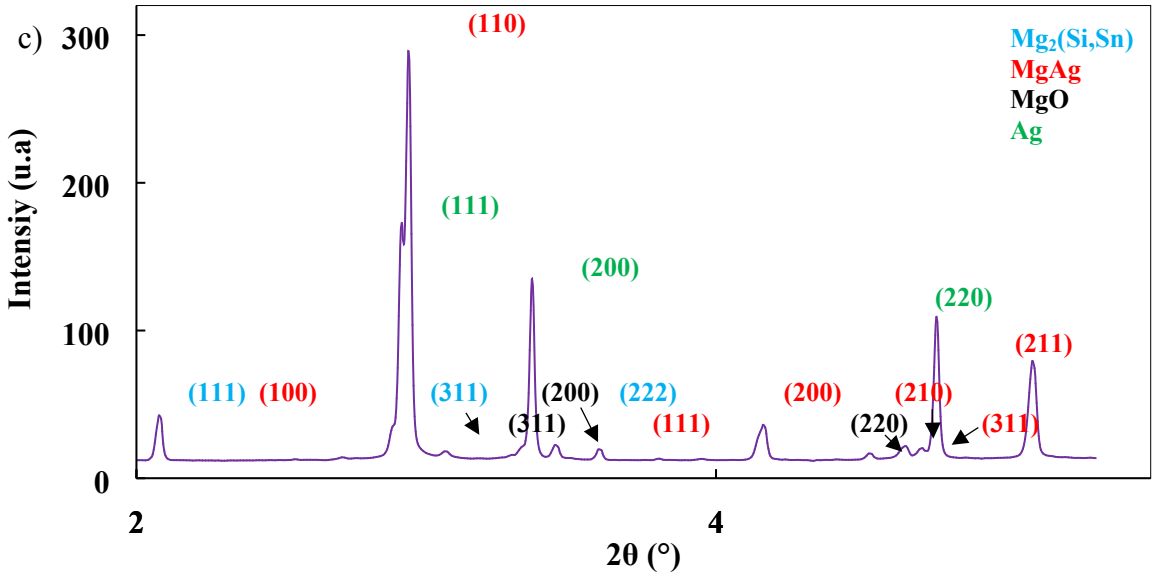

Figure 10.(a) SEM picture of the cross section of the n-type hot side of TEM-06 and (b) zoom of this interface. (c) HEXRD pattern of the n-type hot side of the TEM-06 in the difusion layer (analysis volume was 2 x 300 x 3000 µm³).

Besides the formation of a thin MgO layer (~1 µm), as shown in the Figure 11, cracks (about 600 µm of length) are visible in the hot side zone (below the braze) of the *n*-type leg of TEM-07. The presence of these cracks explains the increase of R_{int}. These cracks are due to the fatigue phenomenon caused by thermal cycling. Such type of behavior was not evidenced during the fixed temperature tests at 350°C. The cracks could be caused by cycling stresses induced by thermal expansion mismatch between the TE material and the metallization and electrode materials. These make the TEM exposed to fatigue failures.

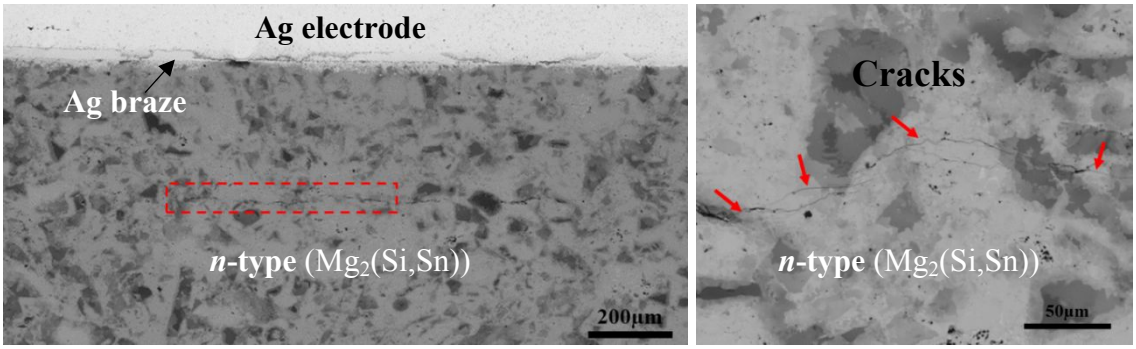

Figure 11. SEM picture of the cross section of n-type hot side of TEM-07. Several cracks are found in the n-type leg nears to the braze (Ag) caused by fatigue. The analysis was performed at the center of the overlap line of the brazed joint.

3.1.2.3. Cycling test with T_{hot}=400°C

In order to increase the thermal stress and to identify its impact, TEM-08 was submitted to 1000 cycles under primary vacuum (a single pump-and-fill step), the temperature at the hot side being varied between 150°C and 400°C. The variations of R_{int} and P_{max} of TEM-08 are reported in Figure 12.a. A monotonous increase of the internal resistance is measured up to 200 cycles, then it increases more rapidly up to 350°C followed by exponential variation up to the failure

of the electrical conduction of the TEM. On the other hand, the increase of R_{int} is accompanied by similar decrease steps of P_{max}.

As shown in Figure 12.b, the *n*-type TE legs are totally degraded, especially at the hot interface, signature of the "pesting" phenomena observed before. A thick MgO oxide layer has been formed at the hot interface accompanied by cracks that fragment the TEs legs. The *p*-type TE legs are still intact and show chemical and mechanical stability. After more than 600 cycles, the TEM do not produce anymore electrical power. It is clear that at 400°C under primary vacuum, the residual oxygen is sufficient to generate the formation of MgO and the kinetics is accelerated compared to 350°C.

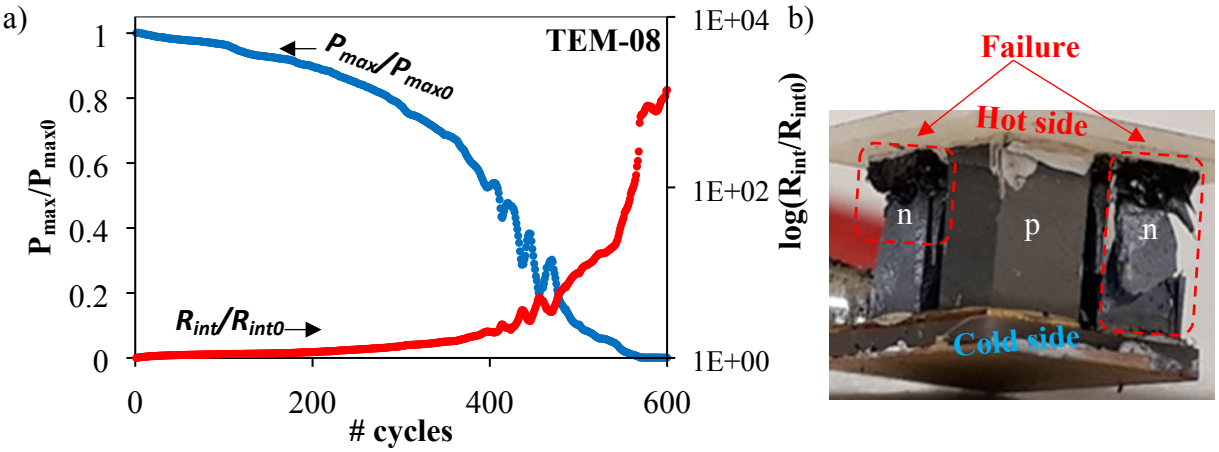

Figure 12. (a) Variation of R_{int} (red) and P_{max} (blue) during the thermal cycling gradient tests of TEM-08 (T_{hot}= 150°-400°C & T_{cold} = 50°C). (b) TEM-08 after the reliability test.

One common mode of failure in power modules is thermal fatigue caused by thermal cycling [50]. When a TEM is subjected to temperature cycles, the thermal expansion and contraction of the different components (TE legs, braze, ceramic substrate, electrode) can lead to cracking or/and delamination, which can ultimately result in reduced performance or complete failure of the TEM. Another mode of failure is due to mechanical stress caused by thermal expansion or vibration. This can result in the deformation or/and fracture of the TEM components (eg: TE legs), leading to reduced performance or complete failure.

3.1. Contact resistances

Table 2 displays the contact resistances (electrode (Cu) / *n*-type and electrode (Cu) / *p*-type) values of the reference and aged samples after 100 hours at 350°C under ambient atmosphere. The thermal test at 350°C for 100 hours leads to an increase of the Cu/*n*-type contact resistance by 2.5 times. This increase is due to the formation of MgO at the Cu/n-type interface as observed by XRD and SEM and as well increases the internal resistance of the TEM-02 as it is observed in figure 5. Using a linear temperature gradient from 350°C to 50°C through the legs and taking into consideration the evolution with temperature of the resistivity described in [15] for each TE

material, a mathematical integration allowed to calculate the resistance of the *n* and *p*-type legs without the contribution of the contacts. Resistances of 0.0142 Ω and 0.0041 Ω by leg are obtained for the HMS and $Mg_2(Si,Sn)$ materials, respectively.

Table 2. Values of the contact resistances (Cu/p and Cu/n) of the reference and aged samples.

	Reference	Aged 350°C-100h
$Rc_{Cu/p}$ [µOhm.cm²]	390	350
$Rc_{Cu/n}$ [µOhm.cm²]	360	790

To calculate the internal resistance of the TEM, the contact resistances were taken into consideration according to the $R = R_c/S$ relation and the values obtained from the experimental contact resistance measurements. For the reference (unaged) TEM, the internal resistance is :

$$R_{int,0} = 2R_n + 2R_p + 4R_{n/Cu} + 4R_{p/Cu} \quad (1)$$

which is equal to 0.0709 Ω. Supposing a full reversibility of the transport properties of the *n* and *p* legs, the R_{int} almost becomes, for an aged TEM at 350°during 100 hours:

$$R_{int} \approx 2R_n + 2R_p + 2R_{n/Cu} + 2R_{n/Cu-aged} + 4R_{p/Cu} \quad (2)$$

(considering that the cold side at the *n*-type/Cu contacts does not evolves) which gives a R_{int} value of 0.0831 Ω. The absolute variation $R_{int}/R_{int,0}$ is equal to 1.17. This ratio is very close to the experimental value obtained in the same condition (1.17). As a conclusion, the ageing evolution of the R_{int} of the TEM at 350°C for 100 hours is mainly due to the evolution of the contact resistance between the *n* type $Mg_2(Si,Sn)$ and the copper in agreement with the formation of the MgO and MgAg phases at this interface.

4. Conclusion

Reliability tests were conducted on several silicide-based TEM. Two types of tests, under fixed and cycling thermal gradients were performed to reveal the different failure modes and to test the robustness of the TEM. The results show that our current TEM resist at a fixed hot side temperature of 250°C under ambient atmosphere for 500 hours and/or to 1000 thermal cycles. Nevertheless, this temperature remains too low to take full advantage of the TE properties of the silicide materials used which the maximum delivered power by the TEM is around 0.21 W/cm^2(per module area).

When increasing the hot side temperature to 350°C, diffusion phenomena are detected at the interface of the hot side of the *n*-type TE material. Pesting phenomena appear leading to the failure of the TEM after a few hundred hours of test. These phenomena are strongly slowed down when the TEM performances are tested under primary vacuum, highlighting the predominant role of oxygen in this mechanism. For T_{hot} = 350°C under primary vacuum, the maximum delivered power by the TEM reach 0.51 W/cm^2(per module area).

For thermal cycling tests with T_{hot}=350°C under vacuum, cracks are observed on the hot side of the n-type legs. These hard-operating conditions result in thermo-mechanical stresses caused by the thermal expansion mismatch between all materials at the hot side of TEM. These make the TEM exposed to fatigue failures like cracks which increase drastically the internal resistance of the TEM.

To be more reliable with a higher lifetime, it is necessary to optimize the $Mg_2(Si,Sn)$ manufacturing to avoid pesting phenomena. Encapsulation or coatings to prevent oxygen diffusion are possible solutions to protect the TEM from pesting effects. For diffusion phenomena at the hot side, diffusion barriers could be developed with a functional material with a high chemical stability to avoid oxidation.

Acknowledgments

This Project was funded by the French National Research Agency (ANR-16-CE05-0012-03). Authors would like to thank the partners from the company HotBlock OnBoard for suppling TEM and CEA-LITEN lab for performing reliability tests. Authors gratefully acknowledge the Deutsches Elektronen-Synchrotron (DESY-Petra III, Hamburg, Germany) for provision of beamtime at the PETRA P07EH2 beamline.

Author Contributions

M. Mejri: Methodology, Investigation, Validation, Writing - original draft.

K. Romanjek: Methodology, Investigation, Validation, review & editing, Supervision, Project administration.

H.Ihou Mouko: Methodology, Investigation, Validation, review & editing, Supervision,, Project administration.

Y. Thimont: Methodology, Investigation, Validation, review & editing, Supervision.

M. Oulfarsi: Methodology, Investigation, Validation, review & editing.

N. David: Methodology, Investigation, Validation, review & editing, Supervision.

B. Malard: Methodology, Investigation, Validation, review & editing, Supervision.

C. Estournès: Methodology, Investigation, Validation, review & editing, Project administration.

A. Dauscher: Methodology, Investigation, Validation, review & editing, Supervision, Project administration.

References

(1) Shi, X.-L.; Zou, J.; Chen, Z.-G. Advanced Thermoelectric Design: From Materials and Structures to Devices. *Chem. Rev.* **2020**, *120* (15), 7399–7515. https://doi.org/10.1021/acs.chemrev.0c00026.

(2) Mori, T.; Priya, S. Materials for energy harvesting: At the forefront of a new wave. *MRS Bulletin* **2018**, *43* (3), 176–180. https://doi.org/10.1557/mrs.2018.32.

(3) Rowe, D. M. *Thermoelectrics Handbook : Macro to Nano*; CRC Press, 2018. https://doi.org/10.1201/9781420038903.

(4) Champier, D. Thermoelectric Generators: A Review of Applications. *Energy Conversion and Management* **2017**, *140*, 167–181. https://doi.org/10.1016/j.enconman.2017.02.070.

(5) Shin, D.-K.; Jang, K.-W.; Ur, S.-C.; Kim, I.-H. Thermoelectric Properties of Higher Manganese Silicides Prepared by Mechanical Alloying and Hot Pressing. *Journal of Electronic Materials* **2013**, *42* (7), 1756–1761. https://doi.org/10.1007/s11664-012-2415-9.

(6) Gelbstein, Y.; Tunbridge, J.; Dixon, R.; Reece, M. J.; Ning, H.; Gilchrist, R.; Summers, R.; Agote, I.; Lagos, M. A.; Simpson, K.; Rouaud, C.; Feulner, P.; Rivera, S.; Torrecillas, R.; Husband, M.; Crossley, J.; Robinson, I. Physical, Mechanical, and Structural Properties of Highly Efficient Nanostructured n- and p-Silicides for Practical Thermoelectric Applications. *Journal of Elec Materi* **2014**, *43* (6), 1703–1711. https://doi.org/10.1007/s11664-013-2848-9.

(7) Kikuchi, Y.; Nakajo, T.; Hayashi, K.; Miyazaki, Y. High Temperature X-Ray Diffraction Study on Incommensurate Composite Crystal MnSi – (3+1)-Dimensional Superspace Approach. *Journal of Alloys and Compounds* **2014**, *616*, 263–267. https://doi.org/10.1016/j.jallcom.2014.07.106.

(8) Miyazaki, Y.; Igarashi, D.; Hayashi, K.; Kajitani, T.; Yubuta, K. Modulated Crystal Structure of Chimney-Ladder Higher Manganese Silicides MnSi γ ($\gamma \sim 1.74$). *Physical Review B* **2008**, *78* (21). https://doi.org/10.1103/PhysRevB.78.214104.

(9) Yamada, T.; Miyazaki, Y.; Yamane, H. Preparation of Higher Manganese Silicide (HMS) Bulk and Fe-Containing HMS Bulk Using a Na–Si Melt and Their Thermoelectrical Properties. *Thin Solid Films* **2011**, *519* (24), 8524–8527. https://doi.org/10.1016/j.tsf.2011.05.032.

(10) Lee, H.; Kim, G.; Lee, B.; Kim, J.; Choi, S.-M.; Lee, K. H.; Lee, W. Effect of Si Content on the Thermoelectric Transport Properties of Ge-Doped Higher Manganese Silicides. *Scripta Materialia* **2017**, *135*, 72–75. https://doi.org/10.1016/j.scriptamat.2017.03.011.

(11) Song, R. B.; Aizawa, T.; Sun, J. Q. Synthesis of Mg2Si1−xSnx Solid Solutions as Thermoelectric Materials by Bulk Mechanical Alloying and Hot Pressing. *Materials Science and Engineering: B* **2007**, *136* (2–3), 111–117. https://doi.org/10.1016/j.mseb.2006.09.011.

(12) Isachenko, G. N.; Zaĭtsev, V. K.; Fedorov, M. I.; Burkov, A. T.; Gurieva, E. A.; Konstantinov, P. P.; Vedernikov, M. V. Kinetic Properties of P-Mg2Si x Sn1 − x Solid Solutions for $x < 0.4$. *Physics of the Solid State* **2009**, *51* (9), 1796–1799. https://doi.org/10.1134/S1063783409090066.

(13) Kim, G.; Lee, H.; Rim, H. J.; Kim, J.; Kim, K.; Roh, J. W.; Choi, S.-M.; Kim, B.-W.; Lee, K. H.; Lee, W. Dependence of Mechanical and Thermoelectric Properties of Mg2Si-Sn Nanocomposites on Interface Density. *Journal of Alloys and Compounds* **2018**, *769*, 53–58. https://doi.org/10.1016/j.jallcom.2018.07.323.

(14) Skomedal, G.; Holmgren, L.; Middleton, H.; Eremin, I. S.; Isachenko, G. N.; Jaegle, M.; Tarantik, K.; Vlachos, N.; Manoli, M.; Kyratsi, T.; Berthebaud, D.; Dao Truong, N. Y.; Gascoin, F. Design, Assembly and Characterization of Silicide-Based Thermoelectric Modules. *Energy Conversion and Management* **2016**, *110*, 13–21. https://doi.org/10.1016/j.enconman.2015.11.068.

(15) Ihou Mouko, H.; Romanjek, K.; Mejri, M.; Oulfarsi, M.; El Oualid, S.; Malinconi, P.; Thimont, Y.; Malard, B.; Estournès, C.; David, N.; Dauscher, A. Manufacturing and Performances of Silicide-Based Thermoelectric Modules. *Energy Conversion and Management* **2021**, *242*, 114304. https://doi.org/10.1016/j.enconman.2021.114304.

(16) Kaibe, H.; Aoyama, I.; Mukoujima, M.; Kanda, T.; Fujimoto, S.; Kurosawa, T.; Ishimabushi, H.; Ishida, K.; Rauscher, L.; Hata, Y.; Sano, S. Development of Thermoelectric Generating Stacked Modules Aiming for 15% of Conversion Efficiency. In *ICT 2005. 24th International Conference on Thermoelectrics, 2005.*; 2005; pp 242–247. https://doi.org/10.1109/ICT.2005.1519929.

(17) Goyal, G. K.; Dasgupta, T. Fabrication and Testing of Mg2Si1-xSnx Based Thermoelectric Generator Module. *Materials Science and Engineering: B* **2021**, *272*, 115338. https://doi.org/10.1016/j.mseb.2021.115338.

(18) Camut, J.; Müller, E.; de Boor, J. Analyzing the Performance of Thermoelectric Generators with Inhomogeneous Legs: Coupled Material–Device Modelling for Mg2X-Based TEG Prototypes. *Energies* **2023**, *16* (9), 3666. https://doi.org/10.3390/en16093666.

(19) Wieder, A.; Camut, J.; Duparchy, A.; Deshpande, R.; Cowley, A.; Müller, E.; de Boor, J. High-Performance Tellurium-Free Thermoelectric Module for Moderate Temperatures Using α-MgAgSb/Mg2(Si,Sn). *Materials Today Energy* **2023**, *38*, 101420. https://doi.org/10.1016/j.mtener.2023.101420.

(20) Camut, J.; Ziolkowski, P.; Ponnusamy, P.; Stiewe, C.; Mueller, E.; de Boor, J. Efficiency Measurement and Modeling of a High-Performance Mg2(Si,Sn)-Based Thermoelectric Generator. *Advanced Engineering Materials* **2023**, *25* (1), 2200776. https://doi.org/10.1002/adem.202200776.

(21) Yi, S.; Attari, V.; Jeong, M.; Jian, J.; Xue, S.; Wang, H.; Arroyave, R.; Yu, C. Strain-Induced Suppression of the Miscibility Gap in Nanostructured Mg2Si–Mg2Sn Solid Solutions. *J. Mater. Chem. A* **2018**, *6* (36), 17559–17570. https://doi.org/10.1039/C8TA05798B.

(22) Yin, K.; Zhang, Q.; Zheng, Y.; Su, X.; Tang, X.; Uher, C. Thermal Stability of $Mg_2Si_{0.3}Sn_{0.7}$ under Different Heat Treatment Conditions. *Journal of Materials Chemistry C* **2015**, *3* (40), 10381–10387. https://doi.org/10.1039/C5TC01434D.

(23) Søndergaard, M.; Christensen, M.; Borup, K. A.; Yin, H.; Iversen, B. B. Thermal Stability and Thermoelectric Properties of Mg2Si0.4Sn0.6 and Mg2Si0.6Sn0.4. *Journal of Materials Science* **2013**, *48* (5), 2002–2008. https://doi.org/10.1007/s10853-012-6967-0.

(24) Zhang, L.; Chen, X.; Tang, Y.; Shi, L.; Snyder, G. J.; Goodenough, J. B.; Zhou, J. Thermal Stability of $Mg_2Si_{0.4}Sn_{0.6}$ in Inert Gases and Atomic-Layer-Deposited Al_2O_3 Thin Film as a Protective Coating. *Journal of Materials Chemistry A* **2016**, *4* (45), 17726–17731. https://doi.org/10.1039/C6TA07611D.

(25) Sizov, A.; Reardon, H.; Iversen, B. B.; Erhart, P.; Palmqvist, A. E. C. Influence of Phase Separation and Spinodal Decomposition on Microstructure of Mg2Si1–xSnx Alloys. *Crystal Growth & Design* **2019**, *19* (9), 4927–4933. https://doi.org/10.1021/acs.cgd.9b00013.

(26) Yasseri, M.; Sankhla, A.; Kamila, H.; Orenstein, R.; Truong, D. Y. N.; Farahi, N.; de Boor, J.; Mueller, E. Solid Solution Formation in Mg2(Si,Sn) and Shape of the Miscibility Gap. *Acta Materialia* **2020**, *185*, 80–88. https://doi.org/10.1016/j.actamat.2019.11.054.

(27) Mejri, M.; Malard, B.; Thimont, Y.; Romanjek, K.; Ihou Mouko, H.; Estournès, C. Thermal Stability of Mg2Si0.55Sn0.45 for Thermoelectric Applications. *Journal of Alloys and Compounds* **2020**, *846*, 156413. https://doi.org/10.1016/j.jallcom.2020.156413.

(28) Oulfarsi, M.; David, N.; Aranda, L.; Medjahdi, G.; Ihou-Mouko, H.; Dauscher, A. Thermal Stability of Mg2Si0.6Sn0.4 under Oxidation Conditions. *ACS Appl Mater Interfaces* **2023**, *15* (18), 22616–22625. https://doi.org/10.1021/acsami.2c21971.

(29) Suvorova, E. I.; Klechkovskaya, V. V. Precipitates of MnSi Cubic Phase in Tetragonal Mn4Si7 Crystal. *Crystallogr. Rep.* **2013**, *58* (6), 854–861. https://doi.org/10.1134/S1063774513060229.

(30) Knott, H. W.; Mueller, M. H.; Heaton, L. The Crystal Structure of Mn15Si26. *Acta Crystallographica* **1967**, *23* (4), 549–555. https://doi.org/10.1107/S0365110X67003184.

(31) Okada, S.; Shishido, T.; Ishizawa, Y.; Ogawa, M.; Kudou, K.; Fukuda, T.; Lundström, T. Crystal Growth by Molten Metal Flux Method and Properties of Manganese Silicides. *Journal of Alloys and Compounds* **2001**, *317–318*, 315–319. https://doi.org/10.1016/S0925-8388(00)01363-3.

(32) Kawasumi, I.; Sakata, M.; Nishida, I.; Masumoto, K. Crystal Growth of Manganese Silicide, MnSi∼1.73 and Semiconducting Properties of Mn15Si26. *Journal of Materials Science* **1981**, *16* (2), 355–366. https://doi.org/10.1007/BF00738624.

(33) Zou, Z.-Q.; Li, W.-C.; Liang, J.-M.; Wang, D. Self-Organized Growth of Higher Manganese Silicide Nanowires on Si(111), (110) and (001) Surfaces. *Acta Materialia* **2011**, *59* (20), 7473–7479. https://doi.org/10.1016/j.actamat.2011.08.050.

(34) Truong, D. Y. N. Thermoelectric Properties of Higher Manganese Silicides. 211.

(35) Nemoto, T.; Iida, T.; Sato, J.; Sakamoto, T.; Nakajima, T.; Takanashi, Y. Power Generation Characteristics of Mg2Si Uni-Leg Thermoelectric Generator. *Journal of Electronic Materials* **2012**, *41* (6), 1312–1316. https://doi.org/10.1007/s11664-012-1963-3.

(36) Skomedal, G.; Holmgren, L.; Middleton, H.; Eremin, I. S.; Isachenko, G. N.; Jaegle, M.; Tarantik, K.; Vlachos, N.; Manoli, M.; Kyratsi, T.; Berthebaud, D.; Dao Truong, N. Y.; Gascoin, F. Design, Assembly and Characterization of Silicide-Based Thermoelectric Modules. *Energy Conversion and Management* **2016**, *110*, 13–21. https://doi.org/10.1016/j.enconman.2015.11.068.

(37) Miao, Z.; Meng, X.; Zhou, S.; Zhu, M. Thermo-Mechanical Analysis on Thermoelectric Legs Arrangement of Thermoelectric Modules. *Renewable Energy* **2020**, *147*, 2272–2278. https://doi.org/10.1016/j.renene.2019.10.016.

(38) Dupont, L.; Khatir, Z.; Lefebvre, S.; Bontemps, S. Effects of Metallization Thickness of Ceramic Substrates on the Reliability of Power Assemblies under High Temperature Cycling. *Microelectronics Reliability* **2006**, *46* (9–11), 1766–1771. https://doi.org/10.1016/j.microrel.2006.07.057.

(39) DUPONT, L.; Khatir, Z.; Lefebvre, S.; Meuret, R.; PARMENTIER, B.; BONTEMPS, S. Electrical Characterizations and Evaluation of Thermo-Mechanical Stresses of a Power Module Dedicated to High Temperature Applications. In *EPE 2005 - 11th European Conférence on Power Electronics and Applications*; Institute of Electrical and Electronics Engineers - IEEE: Dresde, Germany, 2005; p 11p. https://doi.org/10.1109/EPE.2005.219580.

(40) Mejri, M.; Thimont, Y.; Malard, B.; Estournès, C. Characterization of the Thermo-Mechanical Properties of p-Type (MnSi1.77) and n-Type (Mg2Si0.6Sn0.4) Thermoelectric Materials. *Scripta Materialia* **2019**, *172*, 28–32. https://doi.org/10.1016/j.scriptamat.2019.06.037.

(41) Mejri, M.; Malard, B.; Thimont, Y.; Connétable, D.; Floquet, P.; Laloo, R.; Proietti, A.; Estournès, C. Investigation of the Mechanical Properties of MnSi via EBSD-Nanoindentation Coupling and Ab-Initio Calculation. *Journal of Alloys and Compounds* **2022**, *900*, 163458. https://doi.org/10.1016/j.jallcom.2021.163458.

(42) Romanjek, K.; Vesin, S.; Aixala, L.; Baffie, T.; Bernard-Granger, G.; Dufourcq, J. High-Performance Silicon–Germanium-Based Thermoelectric Modules for Gas Exhaust Energy Scavenging. *J. Electron. Mater.* **2015**, *44* (6), 2192–2202. https://doi.org/10.1007/s11664-015-3761-1.

(43) Thimont, Y.; Lognoné, Q.; Goupil, C.; Gascoin, F.; Guilmeau, E. Design of Apparatus for Ni/Mg2Si and Ni/MnSi1.75 Contact Resistance Determination for Thermoelectric Legs. *J. Electron. Mater.* **2014**, *43* (6), 2023–2028. https://doi.org/10.1007/s11664-013-2940-1.

(44) Kieffer, J.; Valls, V.; Blanc, N.; Hennig, C. New Tools for Calibrating Diffraction Setups. *J Synchrotron Rad* **2020**, *27* (2), 558–566. https://doi.org/10.1107/S1600577520000776.

(45) Slim, M. F.; Geandier, G.; Rouillard, F.; Malard, B. Determination of Residual Stress Gradient in a Ti-Stabilized Austenitic Stainless Steel Cladding Candidate after Carburization in Liquid Sodium at 500 °C and 600 °C. *Acta Materialia* **2021**, *221*, 117435. https://doi.org/10.1016/j.actamat.2021.117435.

(46) Slim, M. F.; Geandier, G.; Malard, B.; Rouillard, F. Microstructural and Chemical Changes of a Ti-Stabilized Austenitic Stainless Steel after Exposure to Liquid Sodium at Temperatures between 500 C and 650 C. *Metallurgical and Materials Transactions A* **2021**, *52*, 4438–4453.

(47) Pham, N. H.; Farahi, N.; Kamila, H.; Sankhla, A.; Ayachi, S.; Müller, E.; de Boor, J. Ni and Ag Electrodes for Magnesium Silicide Based Thermoelectric Generators. *Materials Today Energy* **2019**, *11*, 97–105. https://doi.org/10.1016/j.mtener.2018.10.016.

(48) Fitzer, E. Plansee Proc., 2nd Seminar, Reutte/Tyrol. **1955**.

(49) Berkowitz-Mattuck, J. B.; Rossetti, M.; Lee, D. W. Enhanced Oxidation of Molybdenum Disilicide under Tensile Stress: Relation to Pest Mechanisms. *Metall and Materi Trans B* **1970**, *1* (2), 479–483. https://doi.org/10.1007/BF02811558.

(50) Liu, X. W.; Plumbridge, W. J. Thermomechanical Fatigue of Sn–37 Wt.% Pb Model Solder Joints. *Materials Science and Engineering: A* **2003**, *362* (1–2), 309–321.